







RESEARCH ARTICLE OPEN ACCESS

2D Iron Oxide at the Graphene/SiC(0001) Interface

Ryotaro Sakakibara¹  | Tomo-o Terasawa^{2,3}  | Taizo Kawauchi⁴  | Katsuyuki Fukutani^{2,3}  | Takahiro Ito^{5,6}  | Wataru Norimatsu⁷ 

¹Research Center for Materials Nanoarchitectonics (MANA), National Institute for Materials Science (NIMS), Tsukuba, Japan | ²Advanced Science Research Center, Japan Atomic Energy Agency, Tokai, Japan | ³Institute of Industrial Science, The University of Tokyo, Tokyo, Japan | ⁴Isotope Science Center, The University of Tokyo, Tokyo, Japan | ⁵Department of Materials Science and Engineering, Nagoya University, Nagoya, Japan | ⁶Nagoya University Synchrotron Radiation Research Center (NUSR), Nagoya University, Nagoya, Japan | ⁷Faculty of Science and Engineering, Waseda University, Tokyo, Japan

Correspondence: Ryotaro Sakakibara (sakakibara.ryotaro@nims.go.jp)

Received: 20 September 2025 | **Revised:** 22 February 2026 | **Accepted:** 3 March 2026

Keywords: 2D materials | graphene | intercalation | iron oxide | Mössbauer spectroscopy | silicon carbide | transmission electron microscopy

ABSTRACT

Fabrication of two-dimensional (2D) transition-metal oxides has gained considerable attention due to their unique crystal structures and physical properties distinct from their bulk counterparts. Intercalation of foreign elements into the graphene/SiC(0001) interface is a possible approach for achieving this, as it enables the confinement and arrangement of atoms within the 2D interface. However, while various 2D metals and their compounds have been synthesized at the graphene/SiC interface, the fabrication of 2D transition-metal compounds remains challenging. This difficulty arises from the high reactivity of transition metals such as Fe, Co, and Ni, which readily form carbides and silicides with the host material. In this work, the fabrication of a 2D iron oxide at the graphene/SiC interface is demonstrated through the simultaneous intercalation of Fe and O. Direct observation using atomic-resolution electron microscopy revealed that the crystalline 2D iron oxide is encapsulated by graphene and forms a sharp interface with the SiC substrate. Structural analysis and Mössbauer spectroscopy suggest that the 2D iron oxide exhibits a wüstite-like structure. These findings provide another strategy for synthesizing 2D transition-metal oxides, opening new avenues for the advancement of 2D magnetic materials.

1 | Introduction

Two-dimensional (2D) metals and their compounds can exhibit intriguing properties distinct from their bulk counterparts. Due to their potential applications in catalysis, electronics, and other fields, various methodologies have been developed for their synthesis and structural control [1–10]. One promising approach involves utilizing the 2D space between van der Waals (vdW) materials, such as graphene, and their substrates [5–10]. For example, intercalation of a Au monolayer into the graphene/Ni(111) interface [5] defines a path for the exploration of the electronic states of elements confined in a 2D space. A more extensively studied system is epitaxial graphene on SiC(0001) [10–21]. Foreign elements such as Au [11] and Ca [12] can inter-

calate into the vdW gap between graphene and the buffer layer, a carbon reconstruction layer formed by thermal decomposition of SiC(0001). Intercalation into the buffer layer/SiC interface has attracted much more attention [10, 13–21]. In this case, foreign elements saturate the topmost Si atoms of SiC, while the buffer layer is decoupled from SiC and converted into quasi-freestanding monolayer graphene (QFMLG). So far, various elements have been stabilized at this QFMLG/SiC interface [13], such as H [14], O [15, 16], Sn [17], Sb [18], Au [19], Ag [20], and Pb [21]. Furthermore, leveraging this approach, the synthesis of 2D compounds has been reported. For example, Al Balushi et al. synthesized graphene-encapsulated 2D GaN by intercalating Ga into the buffer layer/SiC interface, followed by nitridation [22]. Also, Kakanakova-Georgieva et al. synthesized 2D AlN [23],

This is an open access article under the terms of the [Creative Commons Attribution-NonCommercial](https://creativecommons.org/licenses/by-nc/4.0/) License, which permits use, distribution and reproduction in any medium, provided the original work is properly cited and is not used for commercial purposes.

© 2026 The Author(s). *Small Methods* published by Wiley-VCH GmbH

2D InN [24], and 2D InO [25] at the graphene/SiC interface using a metal-organic chemical vapor deposition process. These 2D compounds exhibit structures and physical properties that are not observed in their bulk forms [22, 24], and therefore, the graphene/SiC interface provides an excellent platform for exploring novel 2D materials.

In this context, the fabrication of 2D compounds based on transition metals such as Fe, Co, and Ni is of great interest, as it could lead to the development of 2D magnetic materials and proximity-induced spin injection into graphene [26, 27]. In recent years, 2D magnetic materials have been shown to exhibit strong magnetic anisotropy and thickness-dependent modulation of magnetism [28, 29], highlighting the importance of dimensional reduction in magnetic materials. At the graphene/SiC interface, a possible strategy for their synthesis is to first intercalate a transition metal, followed by its oxidation or nitridation. However, these transition metals readily react with graphene and SiC to form carbides [30, 31] or silicides [32, 33], which makes intercalation challenging. As a result, despite several attempts [34–36], direct evidence for the fabrication of 2D transition metals and their compounds at the graphene/SiC interface has not been provided to date.

Here, we report the formation of a 2D iron oxide layer at the graphene/SiC interface by the intercalation technique. We investigated the optimal conditions for intercalation and found that intentional oxidation of the Fe thin film deposited on the buffer layer/SiC surface before the intercalation is effective. This approach facilitates the intercalation of Fe and O, and the buffer layer is transformed into QFMLG. As a result, a crystalline 2D iron oxide layer is formed at the graphene/SiC interface. The structure of this interfacial 2D iron oxide was analyzed in detail using atomic-resolution electron microscopy and theoretical calculations. Mössbauer spectroscopy measurements revealed that the interfacial iron oxide exhibits a magnetic transition at a low temperature. Our approach enables the synthesis of 2D magnetic materials at a large scale and their stabilization by graphene encapsulation, which facilitates the study of nanoscale magnetism at the 2D limit.

2 | Results and Discussion

2.1 | Comparison of Two Annealing Methods

We first investigate the optimal condition for intercalation. As the initial sample, we prepared the buffer layer on a SiC(0001) substrate with a size of $5 \times 5 \text{ mm}^2$ by thermal decomposition [37–42]. The buffer layer/SiC sample was loaded into an ultra-high vacuum (UHV) chamber and degassed at around 700°C . Subsequently, an Fe thin film with a nominal thickness of about 4 nm was deposited on the sample surface. Two annealing approaches were compared, as illustrated in Figure 1. In the first method, the sample was annealed in UHV immediately after the deposition of metallic Fe (upper part of the figure). Although this is a typical approach for metal intercalation [17–21, 34–36], it resulted in the formation of multilayer graphene and iron silicide. In the second method, the deposited Fe was oxidized by air exposure and subsequently annealed in UHV (lower part of the figure). We found that this approach leads to the formation

of QFMLG and interfacial 2D iron oxide, as a consequence of intercalation. In both methods, the annealing temperature and duration were set to 660°C – 710°C and 20 min, respectively. In the following, we compare spectroscopic evidence for the two methods to demonstrate that annealing with pre-oxidized Fe enables intercalation.

2.1.1 | Evolution of Raman Spectrum

Raman spectroscopy was employed to investigate the structural evolution of the buffer layer. The Raman spectrum of the initial sample, shown in Figure 2a, exhibits a broad feature in the 1300 – 1600 cm^{-1} range. This spectral feature arises from the vibrational density of states of the buffer layer and differs from the Raman modes of sp^2 -hybridized graphene [43, 44]. A weak signature of the graphene 2D band is also observed near 2720 cm^{-1} [45, 46], suggesting the presence of excess graphene formed during thermal decomposition. To examine the spatial uniformity of the sample, the median Raman spectrum obtained from 100 spectra is presented in Figure S1. The median spectrum exhibits a largely flat 2D-band region, indicating that the surface is mainly covered by the buffer layer, with minor contributions from overgrown monolayer graphene. This interpretation is further supported by an atomic force microscopy (AFM) observation (Figure S2). The topography image reveals the step-terrace structure of the SiC substrate, with step heights of 2–4 nm. Phase contrast imaging indicates that the sample is predominantly covered by the buffer layer, with additional graphene strips nucleated at the step edges [38, 40–42].

After annealing the buffer layer with metallic Fe, the *D*, *G*, and 2D bands characteristic of graphene were observed (Figure 2b) [45, 46]. In general, graphene exhibits *G* and 2D bands at ~ 1560 and $\sim 2680 \text{ cm}^{-1}$, respectively. The *G* band originates from the bond stretching of sp^2 C atoms, while the 2D band arises from the double-resonant Raman scattering process. They provide a means to estimate the number of graphene layers. The *D* band, appearing at $\sim 1360 \text{ cm}^{-1}$, indicates the presence of defects in the graphene lattice. The broad *G* and 2D bands and the sharp *D* band suggest the formation of defect-rich multilayer graphene.

On the other hand, annealing of the buffer layer with pre-oxidized Fe resulted in sharp *G* and 2D bands, with a relatively weak *D* band (Figure 2c). The full width at half maximum (FWHM) of the 2D band was 38 – 55 cm^{-1} , suggesting 1–2 layers of graphene [45, 46]. The defect density estimated from the *D/G* intensity ratio is approximately $1.0 \times 10^{11} \text{ cm}^{-2}$ [47]. Also, the broad feature characteristic of the buffer layer is absent. Mapping of the 2D band FWHM revealed that most of the surface is covered by monolayer graphene, while bilayer graphene appears near the step edges (Figure S3). This suggests that intercalation converted the buffer layer into QFMLG, and the additional graphene strips near the step edges into quasi-freestanding bilayer graphene [48, 49]. Statistics of the Raman mapping data reveal a linear correlation between the *G*-band and 2D-band positions, with a pronounced variation (Figure S4). Based on established analyses in the literature [50], the graphene layer in this sample is subject to a wide range of compressive strain (0%–1%). This may arise from contributions of nonintercalated overgrown graphene or

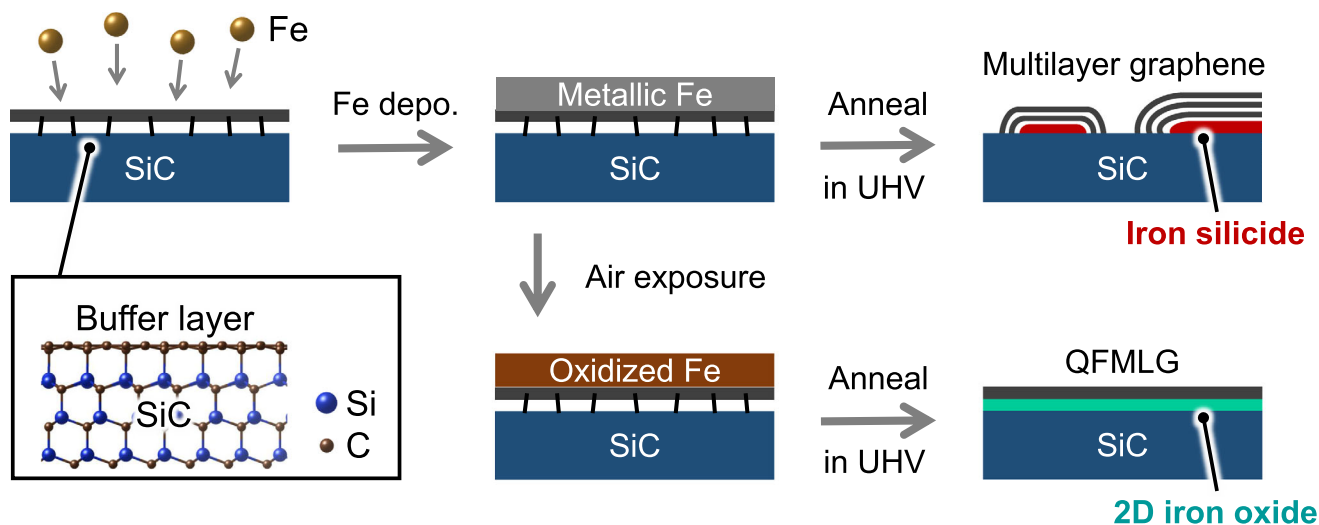


FIGURE 1 | Schematic diagram of the two annealing methods implemented in this study. The atomic structure of the buffer layer/SiC is illustrated as a ball-and-stick model.

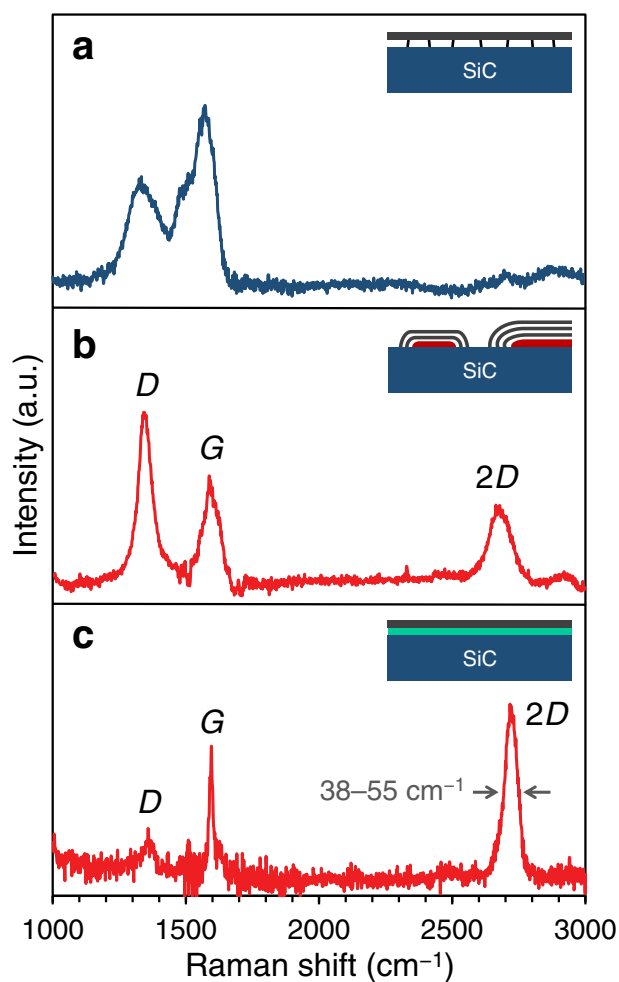


FIGURE 2 | Raman spectra of (a) the initial buffer layer, (b) the sample annealed with metallic Fe, and (c) the sample annealed with pre-oxidized Fe. Note that the contribution of the SiC substrate is subtracted from all Raman spectra.

from interactions between the graphene layer and residual iron oxide on the surface.

2.1.2 | Evolution of XPS Spectra

The C 1s X-ray photoemission spectroscopy (XPS) spectrum of the initial sample (Figure 3a) is mainly explained by two peaks from the buffer layer (S1 and S2), one peak from overgrown monolayer graphene (dotted line), and one peak from bulk SiC [16, 18, 20–21, 39–40]. The S1 and S2 peaks originate from C atoms in the buffer layer that are respectively bonded and not bonded to the underlying SiC substrate. As these peaks are known to be separated by about 880 meV with a peak area ratio of 1: 2, the peak fitting was carried out under these constraints. The small component at higher binding energy arises from hydrocarbon contamination [51]. The Si 2p spectrum (Figure 3b) shows contributions from interfacial Si and bulk SiC [19–21]. In the fitting of the Si 2p spectrum, a spin-orbit splitting of 0.6 eV was employed, and the area ratio of the $2p_{1/2}$ to $2p_{3/2}$ components was constrained to 1: 2. Fitting parameters for the C 1s and Si 2p spectra are summarized in Tables S1 and S2, respectively. For the Fe 2p spectrum, no signal was identified (Figure 3c). These results indicate that the surface of the initial sample is mainly covered by the buffer layer, as illustrated in Figure 3d.

After annealing the buffer layer with metallic Fe, the C 1s spectrum exhibits the graphene-derived peak and the bulk SiC component (Figure 3e). Additionally, the Si 2p spectrum in Figure 3f shows a new peak at around 99.8 eV, which is indicative of Si–Fe bonding [52]. The Fe 2p spectrum exhibits spin-orbit split $2p_{1/2}$ and $2p_{3/2}$ peaks, each of which consists of two main components (Figure 3g). The sharp peaks at lower binding energy, indicated by the arrows, can be attributed to iron silicide [52], whereas the broad peaks at higher binding energy arise from residual iron(III) oxide formed after sample preparation. Note, since deconvolution of Fe 2p spectra is nontrivial due to strong multiplet splitting and satellite features [53, 54], we here limited our analysis to the overall spectral shape. Together with the

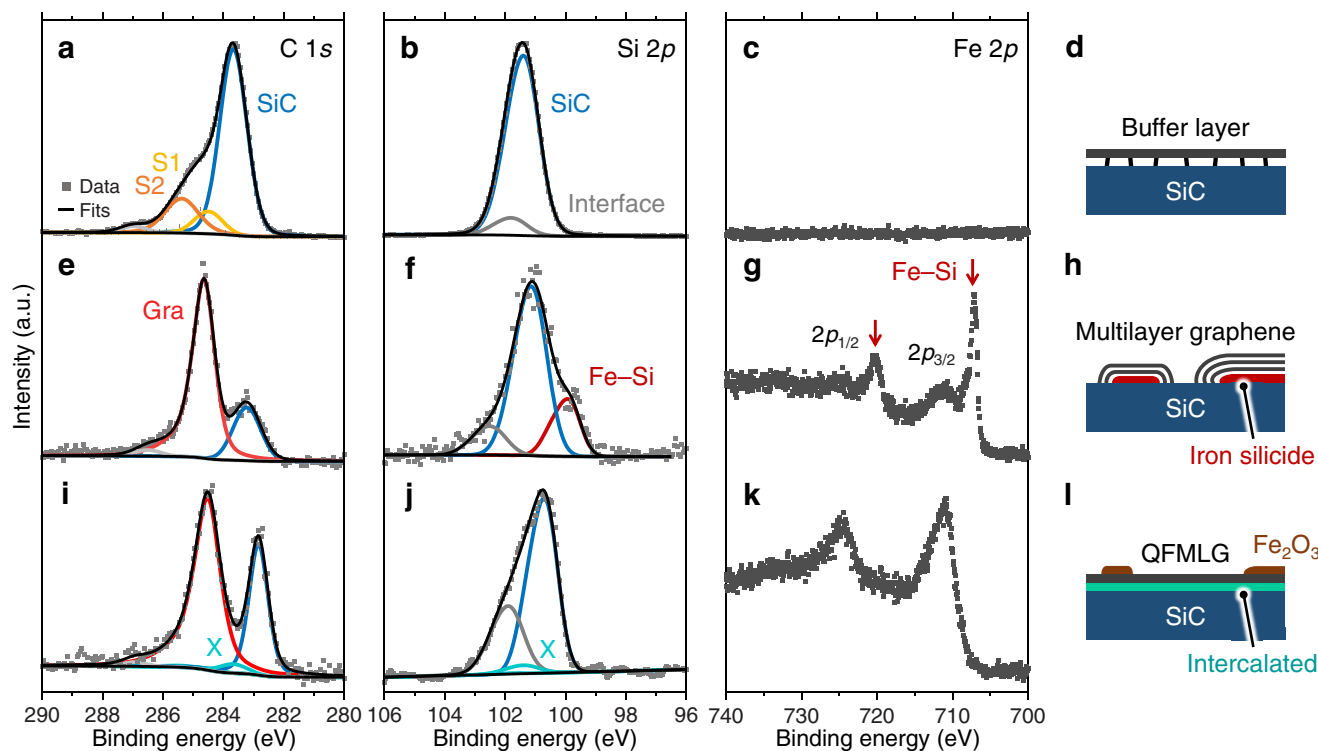


FIGURE 3 | Evolution of XPS spectra. (a–c) C 1s, Si 2p, and Fe 2p core-level spectra of the initial sample, with (d) its schematic illustration. (e–g) The spectra after annealing with metallic Fe, showing the formation of multilayer graphene and iron silicide, as illustrated in (h). (i–k) The spectra after annealing with pre-oxidized Fe, reflecting the conversion of the buffer layer into QFMLG via intercalation, as illustrated in (l). Fitting of the C 1s and Si 2p spectra was performed after Shirley's background subtraction, while the Fe 2p spectra are shown as raw data.

Raman spectroscopy results, we conclude that annealing of the buffer layer with metallic Fe led to the formation of defect-rich multilayer graphene and iron silicide on the sample surface (Figure 3h).

After annealing the buffer layer with pre-oxidized Fe, the C 1s spectrum also exhibits the graphene-derived peak (Figure 3i), but its intensity relative to the SiC component is substantially lower than that in Figure 3e. The small component X accounts for the non-intercalated region, which was fitted by scaling down the line shape of Figure 3a. The Si 2p spectrum in Figure 3j does not show any indication of iron silicide. As in the C 1s case, the small component X reflects the non-intercalated region. Furthermore, in both the C 1s and Si 2p spectra, the bulk SiC component shifted to lower binding energy by about 0.7 eV. This shift is commonly associated with the intercalation of a foreign element [20, 21], which results from the band bending due to the termination of interfacial Si with other elements. Consistent with the Raman spectroscopy results, these findings support the intercalation-induced conversion of the buffer layer into QFMLG. In the Fe 2p spectrum in Figure 3k, broad peaks of iron(III) oxide were observed. As evidenced by electron microscopy observations presented later, this spectrum contains contributions from both the interfacial component and residual surface iron oxide (Figure 3l). By optimizing the amount of deposited Fe, further insight into the chemical states and stoichiometry of the intercalated phase could be obtained by XPS. Nonetheless, a tentative deconvolution of the spectrum was performed based on assumed chemical compositions for these two components, considering multiplet splitting (Figure S5 and Table S3) [53, 54]. The fitting result

suggests that a non-negligible amount of Fe₂O₃ residue remains on the surface.

2.1.3 | Atomic-Scale Observation of the Interface

Figure 4a shows a cross-sectional high-resolution transmission electron microscopy (HR-TEM) image of the sample annealed with metallic Fe, with electron incidence parallel to the [1120]_{SiC} direction. The image reveals a layered contrast of multilayer graphene, as well as an island-like structure beneath it. Figure 4b presents a corresponding high-angle annular dark field scanning TEM (HAADF-STEM) image. The island structure exhibits a bright contrast, suggesting the presence of an element with a higher atomic number than Si and C. As indicated by the black arrow, this island is embedded more than 1 nm below the SiC substrate surface. Such island structures were observed in multiple regions across the sample with a variety of shapes and numbers of graphene layers. Considering the above XPS results, these islands are suggested to be iron silicide. The iron silicide seen in this field of view was further identified as Fe₃Si based on a structural analysis of the TEM image.

Figure 4c shows an HR-TEM image of the sample annealed with pre-oxidized Fe, where the uniform graphene layer is visible on the SiC surface. Interestingly, in the corresponding HAADF-STEM image (Figure 4d), three layers of bright spots are arranged at the graphene/SiC interface. The number of these interface layers was 2–4 in the observed area (Figure S6). We note that, although two layers of graphene are observed in this

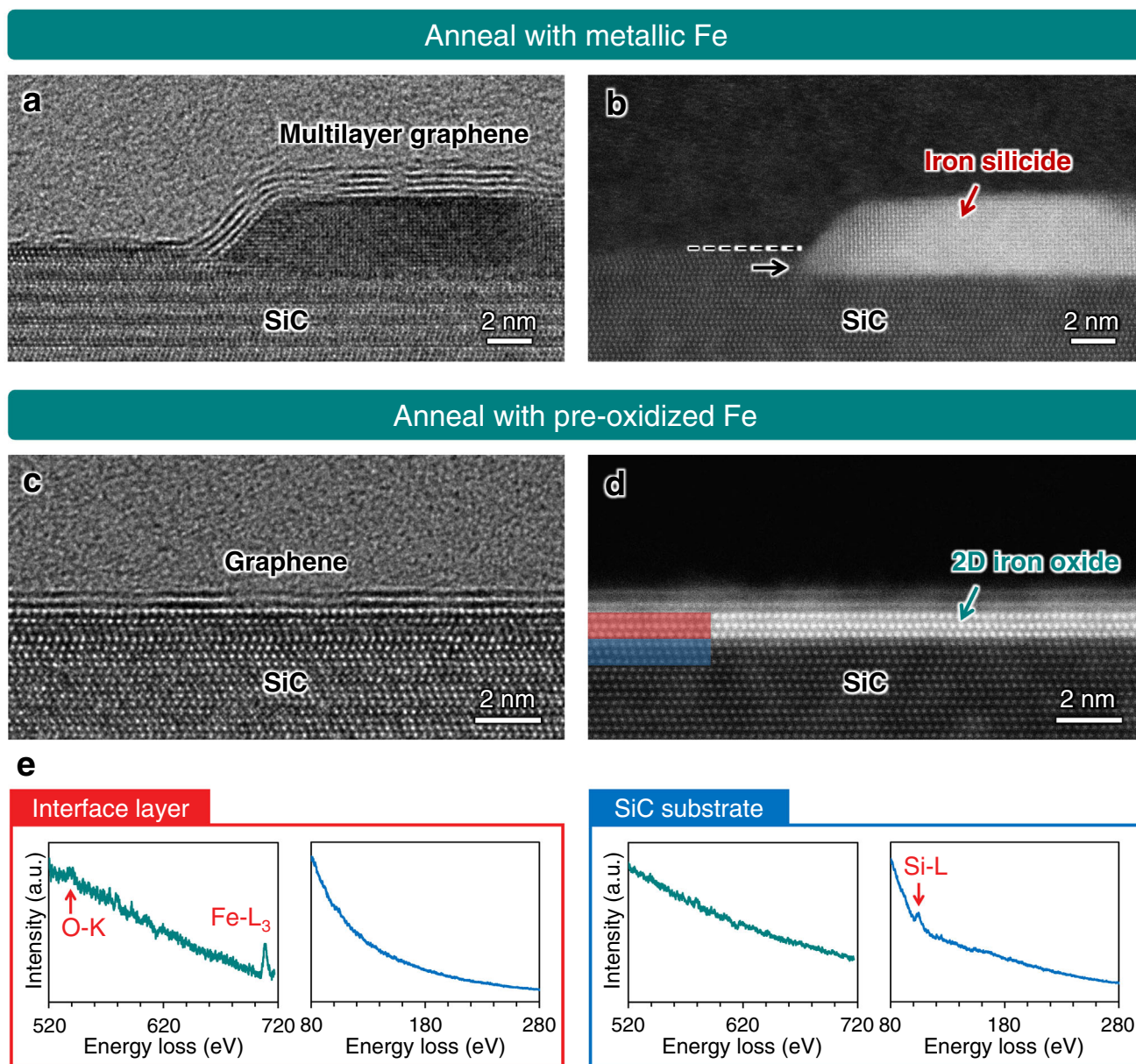


FIGURE 4 | Atomic-scale observation and elemental analysis of the interface. (a,b) Cross-sectional HR-TEM and HAADF-STEM images of the sample annealed with metallic Fe. In (b), the SiC surface and the bottom of the iron silicide island are indicated by a dashed line and a black arrow, respectively. (c,d) Cross-sectional HR-TEM and HAADF-STEM images of the sample annealed with pre-oxidized Fe, confirming uniform graphene formation. In (d), bright spots are arranged at the graphene/SiC interface. (e) EELS spectra acquired from the highlighted regions in (d), showing O-K and Fe-L₃ absorption edges detected only at the interface layer, indicating the formation of 2D iron oxide.

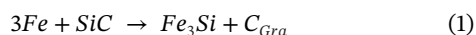
field of view, most of the sample surface is covered by a single layer, as confirmed by Raman mapping (Figure S3). Chemical analysis of the sample interface was performed using electron energy loss spectroscopy (EELS), as shown in Figure 4e. EELS spectra were selectively acquired from the interface layer and the SiC region just beneath it, as indicated by the red and blue rectangles in Figure 4d, respectively. In the interface layer, peaks corresponding to the Fe-L₃ and O-K absorption edges were observed, while no significant signal was detected at the Si-L absorption edge. In contrast, in the SiC region just below the interface layer, neither Fe nor O was detected, but a clear Si peak was observed. These results indicate that the interface layer is composed of Fe and O, and forms a sharp interface with the SiC

substrate. Energy dispersive X-ray spectroscopy (EDS) mapping also confirms the presence of Fe and O at the interface (Figure S7). Based on these analytical results, we conclude that the bright spots correspond to Fe atoms, and the intercalation of Fe and O occurred. Following many previous studies on intercalation [10, 13, 19–25], we refer to this interfacial structure as 2D iron oxide rather than an ultrathin film. Its thickness is limited to a few atomic layers (Figure S6), consistent with previously reported 2D compounds such as 2D GaN [22] and 2D AlN [23]. Note, a low-magnification TEM image reveals numerous residual iron oxide islands on the sample surface, but the graphene/2D iron oxide/SiC structure was preserved beneath these islands (Figure S8).

2.1.4 | Formation Mechanism

Annealing the buffer layer with metallic Fe resulted in the formation of multilayer graphene and iron silicide, whereas annealing with pre-oxidized Fe enabled the intercalation of Fe and O. In both cases, Fe atoms penetrated the buffer layer to reach the underlying SiC. Direct penetration of Fe atoms through the hexagonal lattice of the buffer layer is unlikely, given that even a H atom requires a penetration barrier of 2.55 eV [55]. Thus, the penetration of Fe atoms is most likely assisted by intrinsic vacancy defects [56] and/or local lattice disruption. This interpretation is consistent with the observation of graphene *D* bands in the Raman spectra (Figure 2b,c). Since such defects are thought to be more abundant at step edges than on terraces, penetration may occur preferentially at step edges [57]. Indeed, for annealing with pre-oxidized Fe, a HAADF-STEM image reveals bright spots of Fe atoms only at the step edges (Figure S9).

In the following, we discuss the thermodynamics of interfacial reactions after penetration to rationalize the different outcomes of the two annealing methods. The formation of multilayer graphene and iron silicide after annealing with metallic Fe can be explained by the following solid-state reaction:



The enthalpies of formation of SiC and Fe₃Si are −71.4 and −94.1 kJ mol^{−1}, respectively, yielding a Gibbs free energy change of −33 kJ mol^{−1} at 710°C [58]. This indicates that the reaction is thermodynamically favorable under the present experimental conditions. The released C atoms, which have low solubility in iron silicides [59], precipitate on the surface as graphite. Here, iron carbide (Fe₃C) formation is unfavorable because it is metastable, with a positive enthalpy of formation (25.5 kJ mol^{−1}) [58].

On the other hand, the formation of Fe₃Si is significantly suppressed in the presence of oxygen [60, 61], due to the much lower enthalpy of formation of Fe₂O₃ (−824.2 kJ mol^{−1}). In addition, the reported onset temperature for the solid-state reaction between SiC and Fe₂O₃ is approximately 950°C [62], which is above the temperature in our experiment (~710°C). The formation of 2D iron oxide after annealing with pre-oxidized Fe therefore, suggests the presence of an alternative thermodynamic driving force stabilizing the intercalants. A plausible origin is that the termination of unsaturated Si dangling bonds at the buffer layer/SiC interface by O atoms is energetically favorable, facilitating the ordering of Fe and O atoms [10]. Moreover, the graphene/2D iron oxide/SiC structure was observed regardless of the presence or absence of residual iron oxide islands (Figure S8), implying that Fe and O intercalants underwent lateral migration along the interface after initial penetration. Such facile lateral migration has been theoretically demonstrated for other intercalants such as H and Pb, with energy barriers well below 1 eV [55, 63]. Elucidating a more detailed mechanism will require theoretical investigations, as intercalation generally involves complex elementary processes [63] and results in structures that do not exist in the bulk form.

2.2 | Electronic Structure of QFMLG

The low-energy electron diffraction (LEED) pattern of the intercalated sample shown in Figure 5a exhibits six-fold symmetric spots from graphene (red arrow) and a (1 × 1)_{SiC} periodicity (green arrow), with no satellites from the (6√3 × 6√3)R30° reconstruction of the buffer layer [10, 14, 15, 17–21, 37, 39, 40]. The 30° rotation between them indicates that graphene inherits the crystallographic orientation of the buffer layer. The (1 × 1)_{SiC} periodicity suggests the absence of superstructure in the interfacial iron oxide. This observation further highlights the formation of QFMLG through intercalation.

To investigate the electronic structure of this sample, we conducted angle-resolved photoemission spectroscopy (ARPES) measurements at room temperature. The sixfold symmetric map of graphene was clearly observed in the constant energy band at the Fermi energy (Figure 5b). The energy-momentum (*E*-*k*) cut at the \bar{K} point of the Brillouin zone clearly exhibits the characteristic linear dispersion of monolayer graphene (Figure 5c). By extrapolating the two bands in the figure, the Dirac point was estimated to be approximately +0.26 eV relative to the Fermi energy (*E_F*), indicating uniform hole-doping. Here, in epitaxial graphene on SiC obtained by thermal decomposition, the Dirac point is located at −0.4 eV relative to *E_F* (Figure S10) [42]. This electron doping is generally understood as the charge transfer from the buffer layer to the overlying graphene [64]. Upon intercalation, however, the doping level can be drastically altered. For example, H-intercalation induces p-type doping [64], with the Dirac point shifted to +0.30 eV. These results highlight that the position of the Dirac point is sensitive to the chemical state at the interface, as also reported for the intercalation in graphene/metal interfaces [5, 65]. Therefore, the observed Dirac point at +0.26 eV in our sample is likely due to charge transfer from the interfacial iron oxide layer to QFMLG.

Figure 5d–e presents the second-derivative images of the obtained band structures. In addition to the graphene's π band, a broad feature attributed to Fe 3*d* electrons [66] is observed around −1.2 eV across the entire Brillouin zone, which has no clear dispersion relation. A similar localized Fe state has also been reported for Fe intercalation in the graphene/Ir(111) system, [65] supporting the assignment of this feature to an interfacial component. The absence of hybridization between the Fe 3*d* and graphene bands suggests that QFMLG merely serves as a capping layer on the 2D iron oxide. The splitting of these Fe-derived states and their spin characteristics, as well as their possible impact on the spin of graphene electrons via proximity effects, remains to be clarified.

2.3 | Structural Analysis of the Graphene/SiC Interface

Figure 6a,b show HAADF-STEM images, together with intensity profiles along the lateral directions highlighted by the rectangles. In Figure 6a, the bright spots of Fe atoms are aligned along the [1100]_{SiC} direction, with a periodicity of approximately 0.26 nm. As illustrated in the inset, this periodicity matches the spacing of the Si atoms in SiC along the same direction. Figure 6b presents

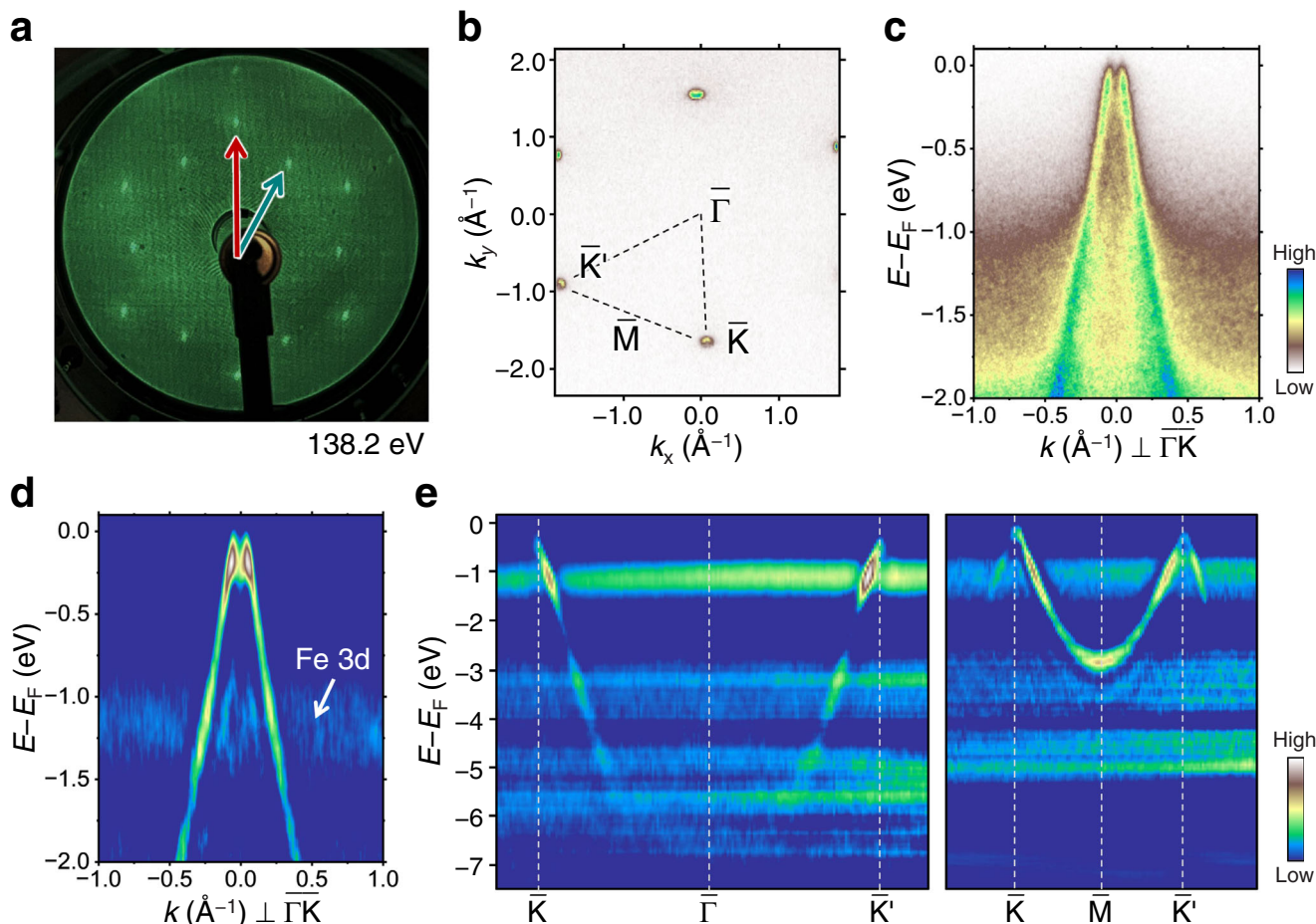


FIGURE 5 | (a) LEED pattern of graphene/2D iron oxide/SiC at 138.2 eV. The red and green arrows indicate the spots from graphene and a $(1 \times 1)_{\text{SiC}}$ periodicity, respectively. (b) ARPES constant energy map at the Fermi energy acquired at a photon energy of 120 eV. (c) E - k dispersion around the K point, acquired at a photon energy of 70 eV. (d) Second derivative image of (c) with respect to energy, revealing an Fe 3d localized state indicated by the arrow. (e) Second derivative images of the E - k cuts along the $\bar{K}-\bar{\Gamma}-\bar{K}'$ and $\bar{K}-\bar{M}-\bar{K}'$ directions in (b), also showing the Fe 3d localized state as well as the graphene's π band.

an image taken from another electron incidence, parallel to the $[1\bar{1}00]_{\text{SiC}}$ direction. Two layers of Fe atoms are observed at the graphene/SiC interface. The intensity profile along the $[11\bar{2}0]_{\text{SiC}}$ direction shows an Fe atom periodicity of about 0.15 nm, which also corresponds to the Si atom periodicity in SiC (inset). Thus, the Fe atoms are considered to form a triangular lattice [17, 19, 20] in each layer, analogous to the arrangement of Si atoms on the SiC(0001) plane. This is in agreement with the LEED results in Figure 5a, where only diffraction spots from graphene and the $(1 \times 1)_{\text{SiC}}$ periodicity were observed. It should be noted that, as seen in Figure 6a, the Fe atoms exhibit an ABA stacking sequence along the c -axis direction.

The interfacial iron oxide consists of layers of Fe atoms arranged in a triangular lattice, with these layers forming an ABA stacking sequence. Merte et al. have proposed a similar 2D iron oxide structure [67], which is composed of two types of building blocks shown in Figure 7a. Specifically, in each layer of the 2D iron oxide, O atoms coordinate around Fe atoms in either tetrahedral or octahedral geometry [67]. Considering all possible combinations of these building blocks, we explored eight structural models to explain the three-layer stacking seen in our STEM observations. For each candi-

date structure, we prepared an iron oxide/4H-SiC(0001) slab model and optimized both the cell size and atomic positions using density functional theory (DFT) calculations. After structural relaxation, six structures either failed to converge or resulted in different atomic configurations, whereas two structures closely matching the STEM images were obtained (Figure 7b,c). Figure 7d presents simulated STEM images based on these structures, both of which qualitatively agree with the experimental image. Also, in both structures, the topmost Si atoms of SiC are bonded to O atoms (Figure 7b,c), which is consistent with the absence of Si-Fe bonding peaks in the XPS Si 2p spectrum (Figure 3j). Accordingly, the interface component around 102 eV can be attributed to Si-O bonding.

A common feature of these two structures is that the iron oxide layer directly above SiC exhibits tetrahedral coordination, reflecting the crystal structure of SiC, while transitioning to octahedral coordination closer to the surface. The octahedral iron oxide layer corresponds to the (111) plane of wüstite, an iron oxide with the NaCl-type structure (Figure 7e). The in-plane Si-Si interatomic distance in the SiC(0001) plane (3.07 Å) and the in-plane Fe-Fe interatomic distance in the

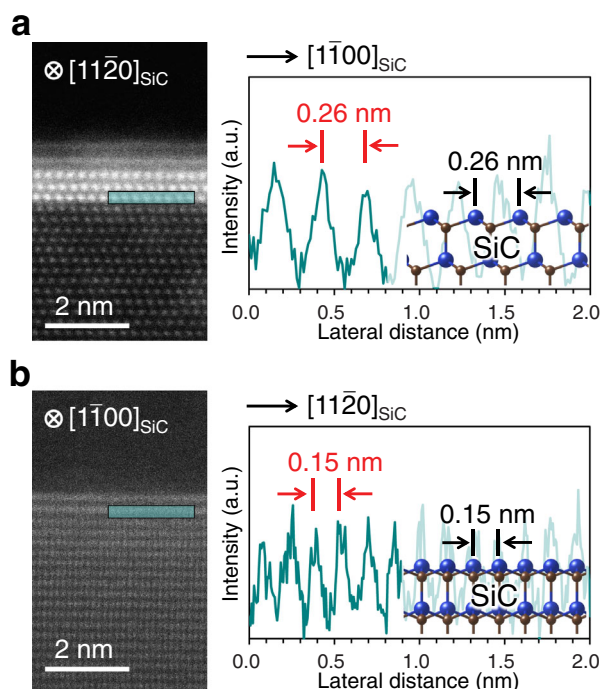


FIGURE 6 | Structural analysis of the graphene/SiC interface. HAADF-STEM images of the same sample with electron incidence parallel to (a) $[11\bar{2}0]_{\text{SiC}}$ and (b) $[1\bar{1}00]_{\text{SiC}}$ directions. The corresponding intensity profiles along the highlighted regions in each image are shown on the right. The bright spots, namely Fe atoms, are considered to be arranged in the same manner as the Si atoms on the SiC(0001) surface.

wüstite (111) plane (3.11 Å) have a mismatch of about 1.3%. Thus, the tetrahedral layer above SiC may serve as a buffer between these two structures. Note that the overlying graphene layer was not considered in these calculations due to the computational cost, and thus, the predicted structures may not fully represent the true stable configurations. Structural optimization and band structure calculations, including the graphene layer, are important for gaining further insight into the properties of the system obtained in this study, and these remain subjects for our future work. In addition, LEED or scanning tunnelling microscopy (STM) studies of the intercalation process would help clarify the structural evolution of the 2D iron oxide and allow a more precise identification of the structure.

2.4 | Magnetic Structure of the Interfacial 2D Iron Oxide

We finally investigated the magnetic properties of the interfacial 2D iron oxide using conversion electron Mössbauer spectroscopy (CEMS). CEMS is a powerful technique for probing the magnetic behavior of ^{57}Fe atoms in materials, based on the observation of the excitation of ^{57}Fe nuclear spin from the $I = 1/2$ ground state to the $I = 3/2$ excited state. We prepared a graphene/2D iron oxide/SiC sample using a ^{57}Fe source and conducted CEMS measurements at room temperature and 100 K (Figure 8a,b). Both spectra were fitted using two components: interfacial iron oxide (red) and α -Fe (green). The α -Fe components exhibit a typical Zeeman-split sextet both at room temperature and

100 K [68] and probably originate from residual Fe remaining on the sample surface. The persistence of metallic iron after air exposure is attributed to the very slow oxidation rate of the high-purity ^{57}Fe source. In addition, the naturally formed iron oxide on these residues is expected to contribute little to the CEMS spectra, likely due to its low crystallinity and a resultant low Lamb-Mössbauer factor [68]. Focusing on the interfacial iron oxide component (red) in the room-temperature spectrum (Figure 8a), a quadrupole-split doublet peak with an isomer shift of about 0.7 mm s^{-1} was observed, while no distinct Zeeman splitting was identified. This suggests that the interfacial 2D iron oxide does not exhibit any magnetically ordered state at room temperature. However, when cooled to 100 K, the doublet peak changed to a Zeeman-split sextet with a magnetic field of 48.5 T, indicating a magnetic ordering (Figure 8b). Such a characteristic magnetic phase transition closely resembles that of wüstite, which undergoes a paramagnetic-to-an antiferromagnetic phase transition upon cooling below its Néel temperature ($\sim 200 \text{ K}$) [69, 70]. The DFT calculations described above indicate that the interfacial 2D iron oxide has a wüstite-like structural aspect. Therefore, our CEMS results can be qualitatively interpreted based on the structural similarity to wüstite. The emergence of antiferromagnetism is also predicted in theoretical studies of 2D Fe_3O_4 structures [67, 71].

The observation of clear magnetic ordering in the interfacial 2D iron oxide is intriguing from the perspective of spin injection into graphene [26, 27]. Spin-resolved ARPES at low temperatures may reveal proximity-induced spin states of graphene electrons. Such spin injection into graphene is particularly attractive for spintronic applications, as it can lead to long spin coherence lengths and high carrier mobility [72]. Finally, the methodology of the present study provides a feasible approach for exploring other 2D magnetic systems that do not exist in the bulk form. The inherently accompanying graphene encapsulation allows the synthesis of otherwise air-sensitive materials. Confinement within the interfacial 2D space enables dimensional reduction of magnetic materials, offering a viable platform to investigate modified magnetic anisotropy and thickness-dependent magnetism.

3 | Conclusions

We compared two approaches toward the synthesis of 2D iron oxide at the graphene/SiC(0001) interface. While the annealing of the buffer layer with metallic Fe led to the formation of defective multilayer graphene and iron silicide, annealing with pre-oxidized Fe intercalated Fe and O into the buffer layer/SiC interface. The QFMLG thus obtained is large-scale and single-oriented, and the interfacial 2D iron oxide forms a sharp interface with the SiC substrate. A detailed analysis of the atomic structure based on STEM observations suggests that the 2D iron oxide has a wüstite-like structural aspect. CEMS measurements revealed a magnetic phase transition in the interfacial 2D iron oxide, which can be associated with the antiferromagnetic behavior of wüstite. The methodology established in the present study provides an alternative route to synthesize large-scale 2D transition-metal oxides at a buried interface, thereby enabling

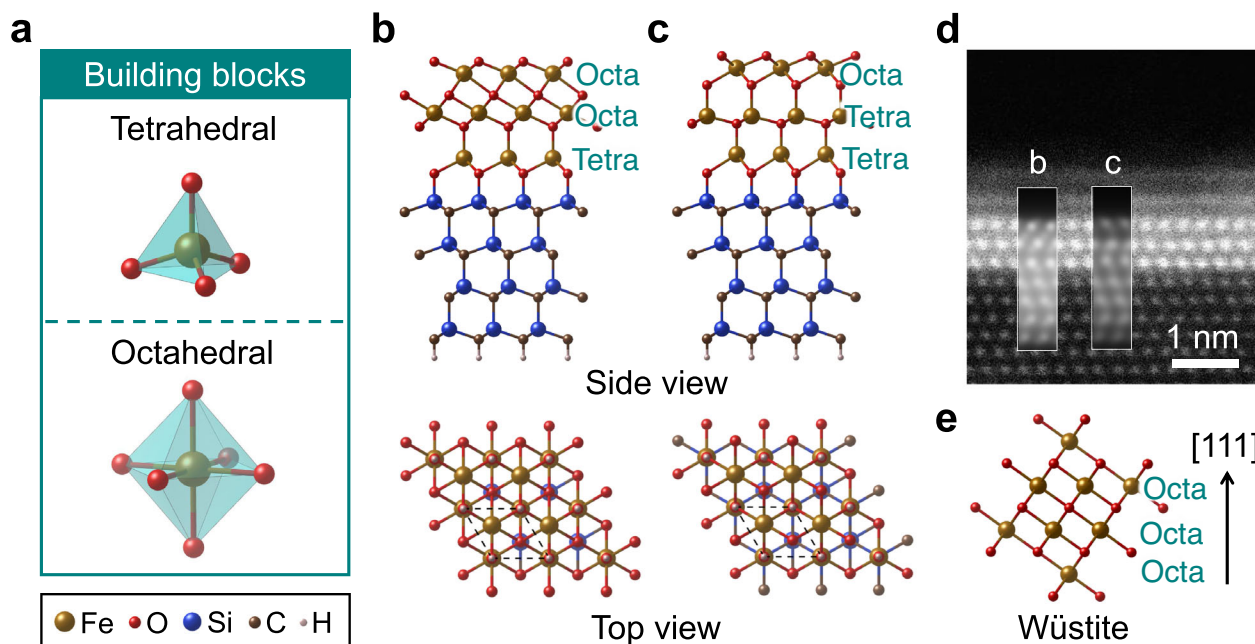


FIGURE 7 | Structures of interfacial 2D iron oxide from DFT calculations. (a) Two types of building blocks compose each iron oxide layer. (b,c) Possible structural models of iron oxide on 4H-SiC(0001), obtained after structural optimization. In the top-view images, unit cells are indicated by dotted rhombuses. (d) Simulated HAADF-STEM images based on the structures of (b) and (c), superimposed on the experimental image. (e) Crystal structure of wüstite.

the exploration and development of diverse nanoscale magnetic materials.

4 | Experimental Section

4.1 | Preparation of the Buffer Layer

A buffer layer sample was prepared by thermal decomposition of SiC [37–42]. A nominally on-axis 4H-SiC(0001) substrate with a size of $5 \times 5 \text{ mm}^2$ was cleaned via ultrasonication in acetone and ethanol, followed by immersion in a hydrofluoric acid solution (20 vol.%) to remove the native oxide layer on the surface. The pre-treated SiC substrate was then annealed at 1500–1600°C in an Ar gas flow atmosphere [48, 49].

4.2 | Deposition of Fe and Subsequent Annealing

The buffer layer sample was loaded into a UHV chamber with a base pressure of approximately 10^{-8} Pa and degassed at around 700°C for 20 min. After cooling to room temperature, Fe was deposited onto the buffer layer surface via molecular beam epitaxy. The Knudsen cell temperature and deposition time were optimized to achieve a nominal film thickness of about 4 nm. Two different annealing methods were employed to investigate the optimal conditions for intercalation. In the first method, the sample was annealed in UHV immediately after the Fe deposition. On the other hand, in the second method, the sample was intentionally exposed to air for overnight to oxidize the deposited Fe film. After the air exposure, the sample was reloaded into the chamber for annealing in UHV. In both methods, the annealing temperature and duration were set to 660–710°C and

20 min, respectively. The ambient pressure during annealing was around 10^{-6} Pa. The samples were transported in air for the following measurements.

4.3 | Raman Spectroscopy

Raman spectroscopy measurements were performed at room temperature using a Renishaw inVia spectrometer. A 532 nm excitation laser with a spot size of about $1 \mu\text{m}^2$ was used. To evaluate the carbon layer on the substrate surface, the SiC substrate contribution is subtracted from all Raman spectra in the main text.

4.4 | AFM

AFM observations were carried out in dynamic force mode to obtain topography and phase images simultaneously. In phase imaging, differences in the viscoelastic properties of the sample surface appear as phase contrasts, allowing the buffer layer and graphene to be distinguished by their different contrasts [48, 49].

4.5 | XPS

XPS measurements were conducted using an Al K_{α} ($h\nu = 1486.6 \text{ eV}$) source with a probe diameter of approximately $500 \mu\text{m}$. Core-level spectra for each element were acquired with an energy step of 0.05 eV and a pass energy of 50 eV. The XPS spectra were analyzed using Shirley's method for background subtraction and Gauss–Lorentz mixing function for peak fitting unless otherwise stated.

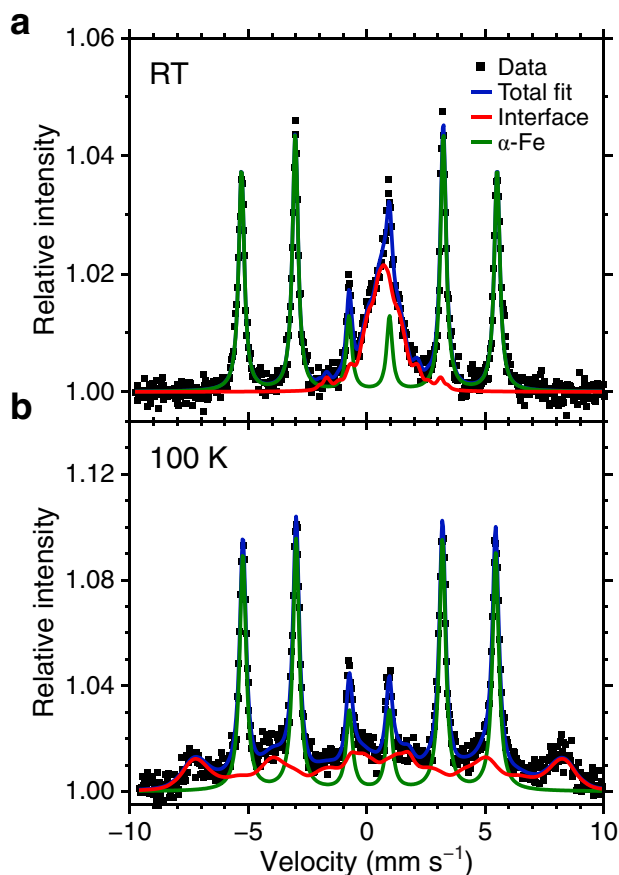


FIGURE 8 | CEMS spectra of the graphene/2D iron oxide/SiC sample measured at (a) room temperature and (b) 100 K. The dots represent the experimental data, while the colored lines indicate the fitting results. The red component corresponds to the interfacial 2D iron oxide, which exhibits a magnetic phase transition upon cooling.

4.6 | Cross-Sectional TEM/STEM

HR-TEM and HAADF-STEM observations were carried out using an aberration-corrected JEM-ARM200F microscope operated at 200 kV. In HAADF-STEM observation, the probe diameter was approximately 70 pm and the detection angle range was 68–280 mrad. Additionally, EELS and EDS were carried out for elemental analysis. Thin specimens for observation were prepared via Ar-ion milling [48, 49].

4.7 | LEED and ARPES

The LEED pattern was taken at an electron energy of 138.2 eV. The ARPES measurements were conducted at room temperature using the beamline BL7U at the Aichi Synchrotron Radiation Center. Photon energies of 70 eV and 120 eV were used, with a spot size of approximately $150 \times 70 \mu\text{m}^2$. The energy resolution was about 40 meV with 0.3° angular resolution.

4.8 | Theoretical Calculations and Simulations

To analyze the interface structure of the obtained sample, DFT calculations were performed using the ABINIT code [73].

The calculations employed the generalized gradient approximation based on the Perdew-Burke-Ernzerhof exchange-correlation functional [74] and norm-conserving pseudopotentials. The iron oxide/4H-SiC(0001) slab models were constructed by fixing Fe atoms at the positions of the bright spots and placing O atoms in either tetrahedral or octahedral coordination. The thickness of the vacuum layer was set to 2 nm, and the bottom carbon atoms of SiC were terminated with hydrogen atoms. A cutoff energy of 30 Ha and a k-point sampling of $4 \times 4 \times 1$ were used for the self-consistent field calculations. Structural optimization was carried out until the residual forces were below 2×10^{-4} Ha Bohr $^{-1}$.

The HAADF-STEM images were simulated using the multi-slice simulation program xHREM. The simulation parameters included an acceleration voltage of 200 kV, a detection angle range of 68–280 mrad, a spherical aberration coefficient of 0.001 mm, and a defocus value of 0 nm.

4.9 | Mössbauer Spectroscopy

The magnetic properties of the sample were investigated by CEMS [68, 75]. Since this technique requires the use of the ^{57}Fe isotope, we first prepared a sample using a ^{57}Fe source following the above procedure. A conventional ^{57}Co radioisotope emitting γ -rays with an energy of 14.413 keV was employed as the γ -ray source. The γ -rays were directed perpendicular to the sample surface. Internal conversion electrons emitted upon the excitation of the ^{57}Fe nuclei were detected using a sealed-off proportional counter filled with rare gases [75]. The measurements were conducted at room temperature and 100 K. An inhomogeneity in the magnetic field was taken into consideration for the spectral fit of the iron oxide component.

Author Contributions

R.S. designed the experiments, performed sample preparation and characterizations (Raman spectroscopy, AFM, XPS, and TEM/STEM), conducted DFT calculations, and analyzed data under the support and direction of T.T. and W.N. T.K. conducted CEMS measurements and analyzed data under the direction of K.F. T.I. conducted LEED and ARPES measurements. R.S. wrote the whole manuscript with input from all authors.

Acknowledgements

We acknowledge K. Yaji, S. Tsuda, F. Arai, and S. Ichinokura at NIMS for their insightful discussions. This work was supported by JSPS KAKENHI Grants Nos. JP22KJ1535, JP25K17917, and JP21K14500. This work was also supported by a Doctoral Research Expense Grant by the Graduate School of Engineering, Nagoya University. This work was partly carried out at the Joint Research Center for Environmentally Conscious Technologies in Materials Science (Project No. 02105) at ZAIKEN, Waseda University. The authors also acknowledge receipt of JAEA Funds at the President's discretion. TEM and STEM observations were carried out at the High Voltage Electron Microscope Laboratory (HVEM) in Nagoya University. The ARPES experiments using synchrotron light were conducted at AichiSR BL7U (Proposal No. 202304112). This work was carried out under the support of the Isotope Science Center, The University of Tokyo.

Conflicts of Interest

The authors declare no conflicts of interest.

Data Availability Statement

The data that support the findings of this study are available from the corresponding author upon reasonable request.

References

1. J. Zhou, J. Lin, X. Huang, et al., “A Library of Atomically Thin Metal Chalcogenides,” *Nature* 556 (2018): 355–359.
2. B. Y. Zhang, K. Xu, Q. Yao, et al., “Hexagonal Metal Oxide Monolayers Derived from the Metal–Gas Interface,” *Nature Materials* 20 (2021): 1073–1078.
3. Z. Zhao, Z. Fang, X. Han, et al., “A General Thermodynamics-Triggered Competitive Growth Model to Guide the Synthesis of Two-Dimensional Nonlayered Materials,” *Nature Communications* 14 (2023): 958.
4. H. Jiang, X. Zhang, K. Chen, et al., “Two-Dimensional Czochochalski Growth of Single-Crystal MoS_2 ,” *Nature Materials* 24 (2025): 188–196.
5. A. Varykhalov, J. Sanchez-Barriga, A. M. Shikin, et al., “Electronic and Magnetic Properties of Quasifreestanding Graphene on Ni,” *Physical Review Letters* 101 (2008): 157601.
6. H.-T. Chin, M. Hofmann, S.-Y. Huang, et al., “Ultra-Thin 2D Transition Metal Monochalcogenide Crystals by Planarized Reactions,” *npj 2D Materials and Applications* 5 (2021): 28.
7. B. Qin, C. Ma, Q. Guo, et al., “Interfacial Epitaxy of Multilayer Rhombohedral Transition-metal Dichalcogenide Single Crystals,” *Science* 385 (2024): 99–104.
8. D. Moon, W. Lee, C. Lim, et al., “Hypotaxy of Wafer-Scale Single-Crystal Transition Metal Dichalcogenides,” *Nature* 638 (2025): 957–964.
9. S. Suzuki, T. Iwasaki, K. K. H. De Silva, et al., “Direct Growth of Germanene at Interfaces between Van der Waals Materials and $\text{Ag}(111)$,” *Advanced Functional Materials* 31 (2021): 2007038.
10. N. Briggs, B. Bersch, Y. Wang, et al., “Atomically Thin Half-van der Waals Metals Enabled by Confinement Heteroepitaxy,” *Nature Materials* 19 (2020): 637–643.
11. B. Premlal, M. Cranney, F. Vonau, et al., “Surface Intercalation of Gold underneath a Graphene Monolayer on SiC (0001) Studied by Scanning Tunneling Microscopy and Spectroscopy,” *Applied Physics Letters* 94 (2009): 263115.
12. Y. Endo, Y. Fukaya, I. Mochizuki, A. Takayama, T. Hyodo, and S. Hasegawa, “Structure of Superconducting Ca-Intercalated Bilayer Graphene/SiC Studied Using Total-Reflection High-Energy Positron Diffraction,” *Carbon* 157 (2020): 857–862.
13. N. Briggs, Z. M. Gebeyehu, A. Vera, et al., “Epitaxial Graphene/Silicon Carbide Intercalation: A Minireview on Graphene Modulation and Unique 2D Materials,” *Nanoscale* 11 (2019): 15440–15447.
14. C. Riedl, C. Coletti, T. Iwasaki, A. A. Zakharov, and U. Starke, “Quasi-Free-Standing Epitaxial Graphene on SiC Obtained by Hydrogen Intercalation,” *Physical Review Letters* 103 (2009): 246804.
15. S. Oida, F. R. McFeely, J. B. Hannon, et al., “Decoupling Graphene from SiC(0001) via Oxidation,” *Physical Review B* 82 (2010): 041411.
16. M. Ostler, R. J. Koch, F. Speck, et al., “Decoupling the Graphene Buffer Layer from SiC (0001) via Interface Oxidation,” *Materials Science Forum* 717–720 (2012): 649–652.
17. S. Hayashi, A. Visikovskiy, T. Kajiwar, et al., “Triangular Lattice Atomic Layer of $\text{Sn}(1 \times 1)$ at Graphene/SiC(0001) Interface,” *Applied Physics Express* 11 (2018): 015202.
18. S. Wolff, S. Roscher, F. Timmermann, et al., “Quasi-Freestanding Graphene on SiC(0001) by Ar-Mediated Intercalation of Antimony: A Route toward Intercalation of High-Vapor-Pressure Elements,” *Annalen der Physik* 531 (2019): 1900199.
19. S. Forti, S. Link, A. Stohr, et al., “Semiconductor to Metal Transition in Two-Dimensional Gold and Its van der Waals Heterostack with Graphene,” *Nature Communications* 11 (2020): 2236.
20. P. Rosenzweig and U. Starke, “Large-Area Synthesis of a Semiconducting Silver Monolayer via Intercalation of Epitaxial Graphene,” *Physical Review B* 101 (2020): 201407.
21. B. Matta, P. Rosenzweig, O. Bolkenbaas, K. Küster, and U. Starke, “Momentum Microscopy of Pb-Intercalated Graphene on SiC: Charge Neutrality and Electronic Structure of Interfacial Pb,” *Physical Review Research* 4 (2022): 023250.
22. Z. Y. Al Balushi, K. Wang, R. K. Ghosh, et al., “Two-Dimensional Gallium Nitride Realized via Graphene Encapsulation,” *Nature Materials* 15 (2016): 1166–1171.
23. A. Kakanakova-Georgieva, G. K. Gueorguiev, D. G. Sangiovanni, et al., “Nanoscale Phenomena Ruling Deposition and Intercalation of AlN at the Graphene/SiC Interface,” *Nanoscale* 12 (2020): 19470–19476.
24. B. Pecz, G. Nicotra, F. Giannazzo, R. Yakimova, A. Koos, and A. Kakanakova-Georgieva, “Indium Nitride at the 2D Limit,” *Advanced Materials* 33 (2021): 2006660.
25. A. Kakanakova-Georgieva, F. Giannazzo, G. Nicotra, et al., “Material Proposal for 2D Indium Oxide,” *Applied Surface Science* 548 (2021): 149275.
26. S. Sarkar, S. Oh, P. J. Newton, et al., “Spin Injection in Graphene Using Ferromagnetic van der Waals Contacts of Indium and Cobalt,” *Nature Electronics* 8 (2025): 215–221.
27. Y. S. Dedkov, M. Fonin, U. Rudiger, and C. Laubschat, “Rashba Effect in the Graphene/n(111) System,” *Physical Review Letters* 100 (2008): 107602.
28. B. Huang, G. Clark, E. Navarro-Moratalla, et al., “Layer-Dependent Ferromagnetism in a van der Waals Crystal down to the Monolayer Limit,” *Nature* 546 (2017): 270–273.
29. H. Wang, H. Lu, Z. Guo, et al., “Interfacial Engineering of Ferromagnetism in Wafer-Scale van der Waals Fe_4GeTe_2 Far above Room Temperature,” *Nature Communications* 14 (2023): 2483.
30. N. A. Vinogradov, A. A. Zakharov, V. Kocovski, et al., “Formation and Structure of Graphene Waves on $\text{Fe}(110)$,” *Physical Review Letters* 109 (2012): 026101.
31. N. A. Vinogradov, K. A. Simonov, A. V. Generalov, et al., “The Structural Evolution of Graphene/ $\text{Fe}(110)$ Systems Upon Annealing,” *Carbon* 111 (2017): 113–120.
32. A. A. Rybkina, S. O. Filnov, A. V. Tarasov, et al., “Quasi-freestanding Graphene on SiC(0001) via Cobalt Intercalation of Zero-Layer Graphene,” *Physical Review B* 104 (2021): 155423.
33. X. Chen and C. Liang, “Transition Metal Silicides: Fundamentals, Preparation and Catalytic Applications,” *Catalysis Science & Technology* 9 (2019): 4785–4820.
34. S. J. Sung, J. W. Yang, P. R. Lee, et al., “Spin-Induced Band Modifications of Graphene through Intercalation of Magnetic Iron Atoms,” *Nanoscale* 6 (2014): 3824–3829.
35. K. Shen, H. Sun, J. Hu, et al., “Fabricating Quasi-Free-Standing Graphene on a SiC(0001) Surface by Steerable Intercalation of Iron,” *The Journal of Physical Chemistry C* 122 (2018): 21484–21492.
36. G. S. Grebenyuk, E. Y. Lobanova, D. A. Smirnov, and I. I. Pronin, “Intercalation of Graphene Formed on Silicon Carbide with Iron, Cobalt and Silicon Atoms,” *Journal of Physics: Conference Series* 1697 (2020): 012105.
37. C. Berger, Z. Song, T. Li, et al., “Ultrathin Epitaxial Graphite: 2D Electron Gas Properties and a Route toward Graphene-Based Nanoelectronics,” *The Journal of Physical Chemistry B* 108 (2004): 19912–19916.
38. C. Virojanadara, M. Syväjärvi, R. Yakimova, L. I. Johansson, A. A. Zakharov, and T. Balasubramanian, “Homogeneous Large-Area Graphene Layer Growth on $6\text{H-SiC}(0001)$,” *Physical Review B* 78 (2008): 245403.
39. K. V. Emtsev, F. Speck, T. Seyller, L. Ley, and J. D. Riley, “Interaction, Growth, and Ordering of Epitaxial Graphene on SiC{0001} Surfaces: A

- Comparative Photoelectron Spectroscopy Study,” *Physical Review B* 77 (2008): 155303.
40. K. V. Emtsev, A. Bostwick, K. Horn, et al., “Towards Wafer-Size Graphene Layers by Atmospheric Pressure Graphitization of Silicon Carbide,” *Nature Materials* 8 (2009): 203–207.
41. W. Norimatsu and M. Kusunoki, “Epitaxial Graphene on SiC{0001}: Advances and Perspectives,” *Physical Chemistry Chemical Physics* 16 (2014): 3501–3511.
42. M. Kusunoki, W. Norimatsu, J. Bao, K. Morita, and U. Starke, “Growth and Features of Epitaxial Graphene on SiC,” *Journal of the Physical Society of Japan* 84 (2015): 121014.
43. F. Fromm, M. H. Oliveira Jr, A. Molina-Sánchez, et al., “Contribution of the Buffer Layer to the Raman Spectrum of Epitaxial Graphene on SiC(0001),” *New Journal of Physics* 15 (2013): 043031.
44. T. Milenov, P. Rafailov, R. Yakimova, I. Shteplyuk, and V. Popov, “Raman Fingerprint of the Graphene Buffer Layer Grown on the Si-Terminated Face of 4H-SiC(0001): Experiment and Theory,” *Journal of Raman Spectroscopy* 55 (2024): 416–424.
45. A. C. Ferrari, “Raman Spectroscopy of Graphene and Graphite: Disorder, Electron–Phonon Coupling, Doping and Nonadiabatic Effects,” *Solid State Communications* 143 (2007): 47–57.
46. A. C. Ferrari and D. M. Basko, “Raman Spectroscopy as a Versatile Tool for Studying the Properties of Graphene,” *Nature Nanotechnology* 8 (2013): 235–246.
47. L. G. Cancado, A. Jorio, E. H. Ferreira, et al., “Quantifying Defects in Graphene via Raman Spectroscopy at Different Excitation Energies,” *Nano Letters* 11 (2011): 3190–3196.
48. J. Bao, W. Norimatsu, H. Iwata, K. Matsuda, T. Ito, and M. Kusunoki, “Synthesis of Freestanding Graphene on SiC by a Rapid-Cooling Technique,” *Physical Review Letters* 117 (2016): 205501.
49. R. Sakakibara and W. Norimatsu, “Microscopic Mechanism of Hydrogen Intercalation: On the Conversion of the Buffer Layer on SiC to Graphene,” *Physical Review B* 105 (2022): 235442.
50. J. E. Lee, G. Ahn, J. Shim, Y. S. Lee, and S. Ryu, “Optical Separation of Mechanical Strain from Charge Doping in Graphene,” *Nature Communications* 3 (2012): 1024.
51. N. Sieber, T. Seyller, L. Ley, et al., “Synchrotron X-ray Photoelectron Spectroscopy Study of Hydrogen-Terminated 6H–SiC{0001} Surfaces,” *Physical Review B* 67 (2003): 205304.
52. N. Ohtsu, M. Oku, K. Satoh, and K. Wagatsuma, “Dependence of Core-level XPS Spectra on Iron Silicide Phase,” *Applied Surface Science* 264 (2013): 219–224.
53. A. Hughes, C. Easton, T. Gengenbach, M. Biesinger, and M. Laleh, “Interpretation of Complex X-Ray Photoelectron Peak Shapes. I. Case Study of Fe 2p_{3/2} Spectra,” *Journal of Vacuum Science & Technology A* 42 (2024): 053205.
54. M. C. Biesinger, B. P. Payne, A. P. Grosvenor, L. W. M. Lau, A. R. Gerson, and R. S. C. Smart, “Resolving Surface Chemical States in XPS Analysis of First Row Transition Metals, Oxides and Hydroxides: Cr, Mn, Fe, Co and Ni,” *Applied Surface Science* 257 (2011): 2717–2730.
55. A. Markevich, R. Jones, S. Öberg, M. J. Rayson, J. P. Goss, and P. R. Briddon, “First-Principles Study of Hydrogen and Fluorine Intercalation into Graphene–SiC(0001) Interface,” *Physical Review B* 86 (2012): 045453.
56. Y. Liu, X. Liu, C.-Z. Wang, et al., “Mechanism of Metal Intercalation Under Graphene through Small Vacancy Defects,” *The Journal of Physical Chemistry C* 125 (2021): 6954–6962.
57. S. Chen, P. A. Thiel, E. Conrad, and M. C. Tringides, “Growth and Stability of Pb Intercalated Phases Under Graphene on SiC,” *Physical Review Materials* 4 (2020): 124005.
58. W. M. Tang, Z. X. Zheng, H. F. Ding, and Z. H. Jin, “A Study of the Solid state Reaction Between Silicon Carbide and Iron,” *Materials Chemistry and Physics* 74 (2002): 258–264.
59. J. C. Schuster, “Silicon Carbide and Transition Metals: A Critical Evaluation of Existing Phase Diagram Data Supplemented by New Experimental Results,” *International Journal of Refractory Metals and Hard Materials* 12 (1993): 173–177.
60. R. C. J. Schiepers, J. A. van Beek, F. J. J. van Loo, and G. de With, “The Interaction between SiC and Ni, Fe, (Fe,Ni) and Steel: Morphology and Kinetics,” *Journal of the European Ceramic Society* 11 (1993): 211–218.
61. H. C. Swart and G. L. P. Berning, “The Effect of Oxygen on the Formation of Iron Silicide,” *Applied Surface Science* 78 (1994): 77–82.
62. Y. Hou, G.-H. Zhang, and K.-C. Chou, “Research on Reaction between SiC and Fe₂O₃,” *Materials Transactions* 59 (2018): 98–103.
63. Y. Han, M. Kolmer, M. C. Tringides, and J. W. Evans, “Thermodynamics and Kinetics of Pb Intercalation under Graphene on SiC(0001),” *Carbon* 205 (2023): 336–344.
64. J. Ristein, S. Mammadov, and T. Seyller, “Origin of Doping in Quasi-free-standing Graphene on Silicon Carbide,” *Physical Review Letters* 108 (2012): 246104.
65. C. Cardoso, G. Avvisati, P. Gargiani, et al., “Magnetic Response and Electronic States of Well Defined Graphene/Fe/Ir(111) Heterostructure,” *Physical Review Materials* 5 (2021): 014405.
66. P. M. Düring, P. Rosenberger, L. Baumgarten, et al., “Tunable 2D Electron- and 2D Hole States Observed at Fe/SrTiO₃ Interfaces,” *Advanced Materials* 36 (2024): 2309217.
67. L. R. Merte, P. A. T. Olsson, M. Shipilin, et al., “Structure of Two-Dimensional Fe₃O₄,” *The Journal of Chemical Physics* 152 (2020): 114705.
68. T. Kawauchi, K. Fukutani, M. Matsumoto, et al., “Surface Magnetic Canting of Iron Films,” *Physical Review B* 84 (2011): 020415.
69. M. Gheisari, M. Mozaffari, M. Acet, and J. Amighian, “Preparation and Investigation of Magnetic Properties of Wüstite Nanoparticles,” *Journal of Magnetism and Magnetic Materials* 320 (2008): 2618–2621.
70. C. A. McCammon and D. C. Price, “Mössbauer Spectra of Fe_xO (x>0.95),” *Physics and Chemistry of Minerals* 11 (1985): 250–254.
71. P. A. T. Olsson, L. R. Merte, and H. Grönbeck, “Stability, Magnetic Order, and Electronic Properties of Ultrathin Fe₃O₄ Nanosheets,” *Physical Review B* 101 (2020): 155426.
72. N. Tombros, C. Jozsa, M. Popinciuc, H. T. Jonkman, and B. J. van Wees, “Electronic Spin Transport and Spin Precession in Single Graphene Layers at Room Temperature,” *Nature* 448 (2007): 571–574.
73. X. Gonze, J. M. Beuken, R. Caracas, et al., “First-principles Computation of Material Properties: The ABINIT Software Project,” *Computational Materials Science* 25 (2002): 478–492.
74. J. P. Perdew, K. Burke, and M. Ernzerhof, “Generalized Gradient Approximation Made Simple,” *Physical Review Letters* 77 (1996): 3865–3868.
75. T. Kawauchi, K. Asakawa, and K. Fukutani, “Sealed-off Helium-Filled Proportional Counter for the Conversion Electron Mössbauer Spectroscopy,” *Hyperfine Interactions* 238 (2017): 75.

Supporting Information

Additional supporting information can be found online in the Supporting Information section.

Supporting File: smtd70599-sup-0001-SuppMat.pdf.